

Influence of Specimen Geometry on Acoustic Emission Signals in Fiber Reinforced Composites: FEM-Simulations and Experiments

Markus G. R. SAUSE, Siegfried HORN

University of Augsburg, Institute for Physics, D-86135 Augsburg, Germany;
markus.sause@physik.uni-augsburg.de, tel. +49 821 5983238, fax +49 821 5983411

Keywords: pattern recognition, finite element simulation, fiber reinforced composites

Abstract

Acoustic emission signals recorded during failure of fiber reinforced composite materials were investigated with pattern recognition techniques to obtain classes of signals each with similar characteristics. Pattern recognition techniques in combination with cluster validity indices allow a fast and valid separation into distinct types of signal classes. A valid correlation of these classes with failure mechanisms in the material is a more difficult task. This is due to the complex formation process of the acoustic emission signal, the dispersive propagation of the excited elastic waves, reflections at the specimen boundaries and to the detection process using a multi-resonant sensor. All these processes alter the inherent acoustic emission signal characteristics associated with a failure mechanism and have to be included in the signal analysis. To better understand the modifications of the acoustic emission signals during propagation and detection we present a finite element simulation approach for three experimental setups used for mechanical testing of fiber reinforced composites. The simulation includes a micromechanical model of the acoustic emission source, an anisotropic propagation medium and a model of a typical broadband acoustic emission sensor. We discuss the influence of the sensors aperture and the changes in its frequency sensitivity. The latter depends on the elastic properties of the material the sensor is in contact with. Further we compare simulations of typical failure mechanisms for geometries of flexural testing, tensile testing and G_{Ic} -testing with the respective acoustic emission signals obtained in the experiment. In all three specimen geometries the inherent characteristics of the source mechanism are distinguishable by characteristic frequency parameters and can be used to identify the failure type.

Introduction

The possibility to identify the occurrence of failure mechanisms in carbon fiber reinforced plastics (CFRP) in dependence of loading is of great practical interest for modern light-weight engineering. Ultimately, the understanding of material failure in CFRP will contribute to optimize the mechanical performance of the composite or reduce its overall weight due to clearly predictable load limits. Acoustic emission (AE) analysis is a powerful tool to monitor micromechanical failure in CFRP. Typically the observed failure consists of inter-fiber matrix cracking, fiber breakage and a variety of interfacial failure mechanisms like fiber-matrix debonding or inter-ply delamination. The possibility to identify these types of failures by suitable interpretation of the recorded AE-signals is an established field of AE-research [1,2,3,4,5,6]. However, due to the dispersive propagation of the excited elastic waves and attenuation effects no generally applicable criterion to identify a particular failure mechanism has been found. Pattern recognition techniques are considered a suitable tool to identify distinct types of AE-signals based on a multitude of features obtained from the recorded signals [3,4,5,6]. The formation of AE-signal clusters depends sensitively on the experimental setup, the geometry of the specimen and the possible existence of other AE-sources not correlated to specimen failure. Therefore, a suitable tool to validate the assignment of distinct AE-signal types to failure mechanisms are finite element simulations of the microscopically observed failure types.

Following the simulation approach by Prosser et al. [7], we recently established a new AE-source model, which takes into account the microscopic elastic properties in the vicinity of the AE-source [6]. It was demonstrated that the results of these simulations compare well to experimental results obtained from a flexural testing geometry with unidirectional ply layout. In the following three typical CFRP geometries and stacking sequences are investigated by such simulations.

Experimental Setup

For the present study three experimental setups typical for mechanical testing of CFRP were used. All specimens were manufactured from the HexPly T800/913 prepreg system using an identical curing cycle. The first setup concerns four-point bending of $(100 \pm 1) \text{ mm} \times (15 \pm 0.5) \text{ mm} \times (1.4 \pm 0.2) \text{ mm}$ (length \times width \times height) specimens exhibiting $[0_5]_{\text{sym}}$ layup according to DIN-EN-ISO 14125. For testing 0.01 mm/s crosshead speed, an inner distance of $(27 \pm 1) \text{ mm}$ and an outer distance of $(81 \pm 2) \text{ mm}$ between supports were used. In a second setup, G_{Ic} specimens with dimensions of $(240 \pm 2) \text{ mm} \times (24 \pm 0.5) \text{ mm} \times (3.0 \pm 0.2) \text{ mm}$ (length \times width \times height) and a $[0_{12}]_{\text{sym}}$ layup were tested according to ASTM D 5528 with a crosshead speed of 10 mm/min. In a third setup tensile loading of specimen geometries with crosshead speed of 1 mm/min was investigated. Here the dimensions were $(170 \pm 2) \text{ mm} \times (40 \pm 0.5) \text{ mm} \times (1.5 \pm 0.1) \text{ mm}$ (length \times width \times height) plates exhibiting a $[0/90_3/0]_{\text{sym}}$ layup with $(55 \pm 1) \text{ mm} \times (40 \pm 0.5) \text{ mm} \times (1.1 \pm 0.1) \text{ mm}$ (length \times width \times height) reinforcements using a $[45/135/0_2]_{\text{sym}}$ layup at the edges as marked in figure 1.

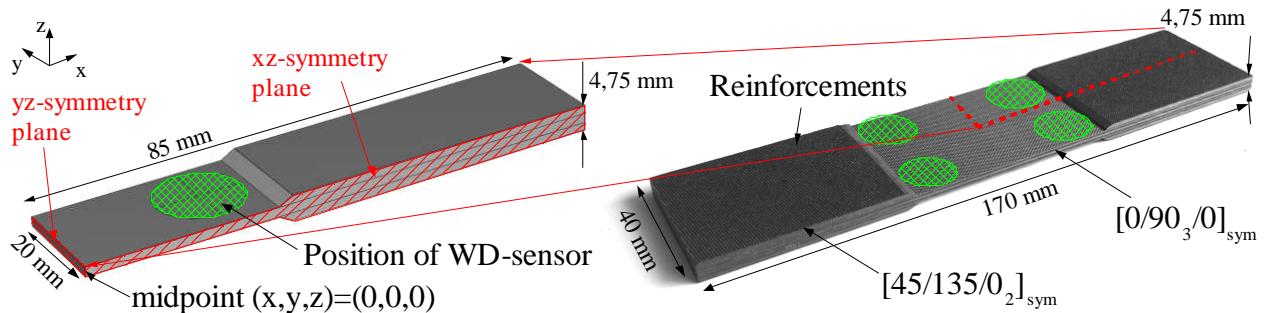


Fig. 1. Experimentally used tensile specimen and corresponding volume for FEM-simulation

All acoustic emission signals were recorded by threshold based triggering using a PCI-2 data acquisition system and the software AEwin with a sampling rate of 10 MS/s. The trigger parameters were optimized to the respective specimen geometries to inhibit triggering of noise signals and reflections from the specimen boundaries. In addition, a bandpass range from 20 kHz to 1 MHz was used to reduce detection of low frequency friction signals and high frequency electromagnetic noise signals. For flexural testing and G_{Ic} -testing, the AE-signals were localized using a hyperbolic localization technique in linear sensor geometry. For the tensile specimens the sensor geometry marked in figure 1 was used for planar localization. In the following only signals, which could be localized, were taken into account for further analysis. For data reduction and postprocessing steps like feature extraction and pattern recognition the software package Noesis was used.

FEM-Simulation of Acoustic Emission Signals

For simulation of the excitation, propagation and the detection of acoustic emission signals the “Structural Mechanics module” of the software package COMSOL was used. For quantitative comparison with experimental data it is necessary to take into account all boundary reflections, which forces the implementation of full scale 3D-simulations. All the simulations made use of symmetry planes as indicated by the red hatched areas in figure 1. This reduces the size of the specimens’ simulated volumes and thus enables faster calculations. The different stacking

sequences were taken into account by respective changes of the elastic coefficients of T800/913 given in table 1 for the unidirectional 0° fiber orientation.

Table 1. Elastic properties of CFRP used for FEM-simulations

	Density [kg/m ³]	Poisson-Ratio	Elasticity Constants [GPa]
Carbon Fiber T800S	1810	0.20	E=294.0
Resin HexPly 913	1230	0.35	E=3.39
T800/913 (unidirectional)	1550	-	C ₁₁ =154.0 C ₁₂ = C ₁₃ =3.7 C ₂₂ = C ₃₃ =9.5 C ₂₃ =5.2 C ₄₄ =2.5 C ₆₆ = C ₅₅ =4.2

Source Model

The AE-source geometry used is shown in a 2D-representation in figure 2 including the dimensions of a “crack”, modeled as three-axis cross cut out of the cracking medium. This enables quasi-independent movement of the “cracks” surfaces in x, y or z direction. For failure the microscopically inhomogeneous elastic properties inherent to CFRP are taken into account by a resin cube surrounding the embedded carbon fiber. These in turn are enclosed in a cube acting as perfectly matched layer (PML). Within this PML the microscopic elastic properties are gradually adjusted to those of the surrounding macroscopic medium (CFRP) in order to provide a continuous transition. Within this source model the effects of orientation between fiber axis and the crack surface movement direction can be included.

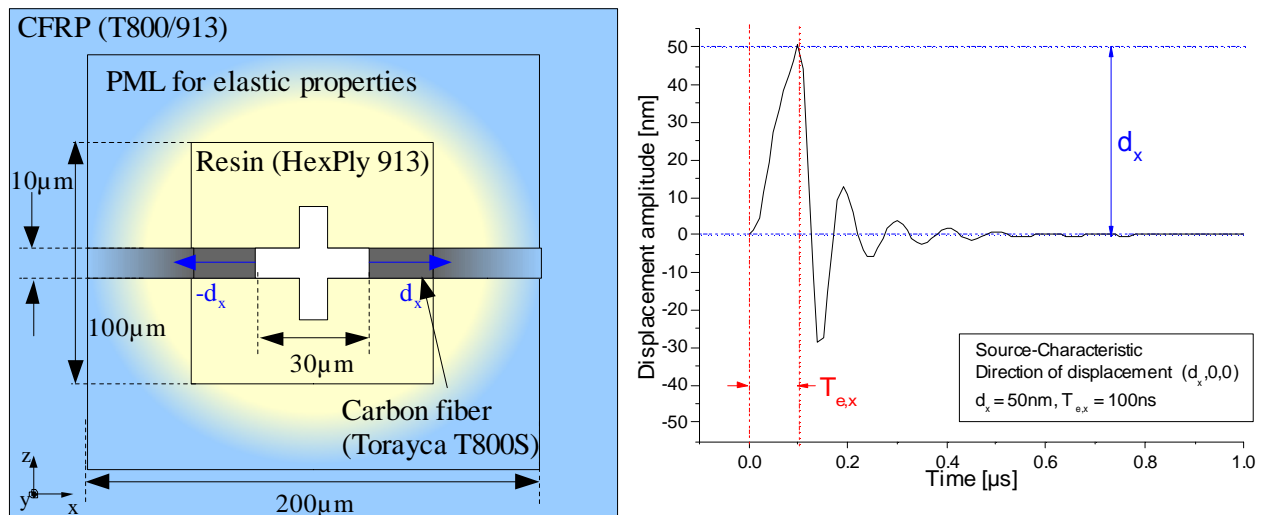


Fig. 2. 2D-representation of source model (left) and typical crack surface oscillation for matrix cracking (right)

In accordance to the considerations of Ohtsu et al. [8], in our model the crack progress is simulated by a linear increasing displacement $d_{(x,y,z)}$ of the crack surface within an excitation time $T_{e,(x,y,z)}$. The subset (x,y,z) indicates the direction of displacement. This results in an oscillatory movement of the cracks surface as shown on the right panel of figure 2. The configuration shown in the left panel of figure 2 refers to simulation of fiber-breakage. Interface failure was simulated introducing additional displacement components directed along the y- and z-axis [6]. For simulation of matrix cracking, the carbon fibers were replaced by respective resin cuboids. Following similar investigations [7,9] a multi-scale approach was chosen with a variable mesh resolution of a maximum value of 1 mm decreasing down to resolutions of 10 μm when

approaching the source. This is required to spatially resolve the excitation process of the acoustic emission source and the subsequent propagation of the elastic wave for the wavelengths associated with the observed frequency range up to 1 MHz. Similarly, the temporal resolution of the model was increased from a resolution of 10 ns during the excitation process ($t < 1 \mu\text{s}$) to a resolution of 100 ns ($t \geq 1 \mu\text{s}$).

As discussed in [6] this results in propagation of Lamb-waves with distinct ratios of zero-order symmetric (S_0) and zero-order antisymmetric (A_0) modes. The ratios of the excited lamb-wave modes show sufficient correlation to the respective source mechanism to be used for their identification by pattern recognition techniques. However, a strong dependency on the source position relative to the specimen edges is observed. As already reported by [10] this can falsify the identification process and has to be taken into account.

Sensor Model

As pointed out by [11] the characteristics of the experimentally detected AE-signals show strong dependence on the used sensor type. For the current investigation the experimentally used type WD-sensor was represented by a full volumetric model as shown in the left panel of figure 3. To demonstrate the accuracy of this sensor model, FEM-simulations of a setup typically used for reciprocity calibration of AE-sensors as described by [12] were performed. This includes piezoelectric conversion of the detected pulses using the material parameters given in table 2. The frequency dependent sensitivity curves obtained by these simulations are shown in the right panel of figure 3 given in dB with reference to $[1\text{V}/\mu\text{bar}]$. These curves are obtained dividing the voltage signals produced by the piezoelectric elements by the respective surface pressure between wear-plate and calibration block. As pointed out by [13] the sensitivity of AE-sensors depend on the material used for the calibration block. For comparison two typical measured sensitivity curves as provided by the manufacturer (Physical Acoustics Corporation) are shown in the right panel of figure 3. The simulated sensitivity curve for a steel block is consistent with experimentally used sensors, which deviate from each other considerably. In particular, the simulation reproduces the magnitude of the signals and shows characteristic differences for the respective material of the calibration block.

Table 2. Elastic properties used for FEM-simulation of type WD-sensor

	Material	Density [kg/m ³]	Poisson- Ratio	Elasticity Constants [GPa]	Coupling constants [C/m ²]	Relative Permittivity
Sensor case	Stainless Steel	7970	0.29	E=219.0	-	-
Backing material	Al-filled Epoxy	2700	0.40	E=30.0	-	-
Acoustic Insulation	PTFE	2200	0.33	E=0.4	-	-
Bonding	Ag-filled Epoxy	1700	0.45	E=2.7	-	-
Wear plate	Al ₂ O ₃	3965	0.22	E=400.0	-	-
Sensor elements	PZT-5A	7750	-	C ₁₁ = C ₂₂ =120.3 C ₁₂ =75.2 C ₁₃ = C ₂₃ =75.1 C ₃₃ =110.9 C ₄₄ =C ₅₅ =21.1 C ₆₆ =22.6	S ₁₃ = -5.4 S ₂₃ = -5.4 S ₃₃ = 15.8 S ₄₂ = 12.3 S ₅₁ = 12.3	$\chi_{11} = 919.1$ $\chi_{22} = 919.1$ $\chi_{33} = 826.6$

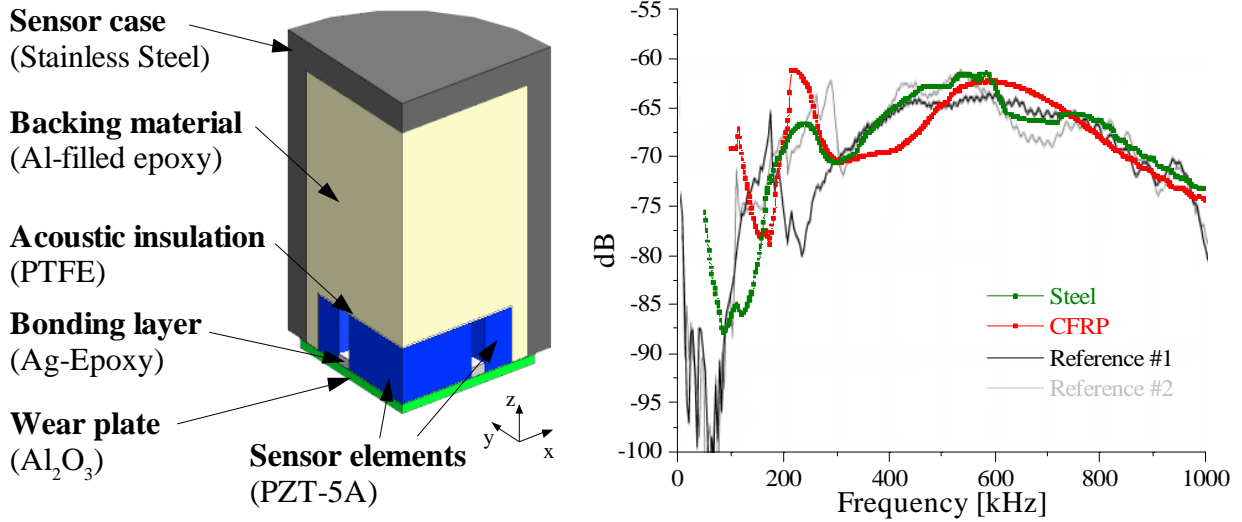


Fig. 3. Quarter volume representation of the used WD-sensor model (left) and comparison of simulated sensitivity curves of the WD-sensor model in dB with reference [1V/μbar] for steel and CFRP blocks with two reference curves (right)

Simulation results

Simulations of matrix-cracking, interface-failure and fiber-breakage were conducted for various source positions on each of the experimentally investigated specimen geometries. As shown in figure 4 simulations of the different failure mechanisms at the respective specimens midpoint position $(x, y, z) = (0, 0, 0)$ produce similar frequency characteristics. For comparison the frequency spectra magnitudes were normalized to their integrated intensity. Typically for matrix cracking low intensity S_0 -modes and high A_0 -modes are observed in the time domain. Since the S_0 -modes in the investigated specimens typically contains higher frequency contributions than the A_0 -modes, this results in dominant contributions at frequencies below 400 kHz. In contrast fiber-breakage results in intense S_0 -modes, which are responsible for the observed dominant frequency weight above 400 kHz. For interface failure the intensity of S_0 - and A_0 -modes is comparable and, consequently, frequency spectra with noticeable contributions above and below 400 kHz are observed. Different stacking sequences and boundary conditions determined by the specimen geometry result in characteristic differences between the respective frequency spectra resulting from the same failure mechanism. These differences are due to the fact, that the AE-signal detected at the sensor position is a superposition of the primary signal and its reflections from the specimen boundaries.

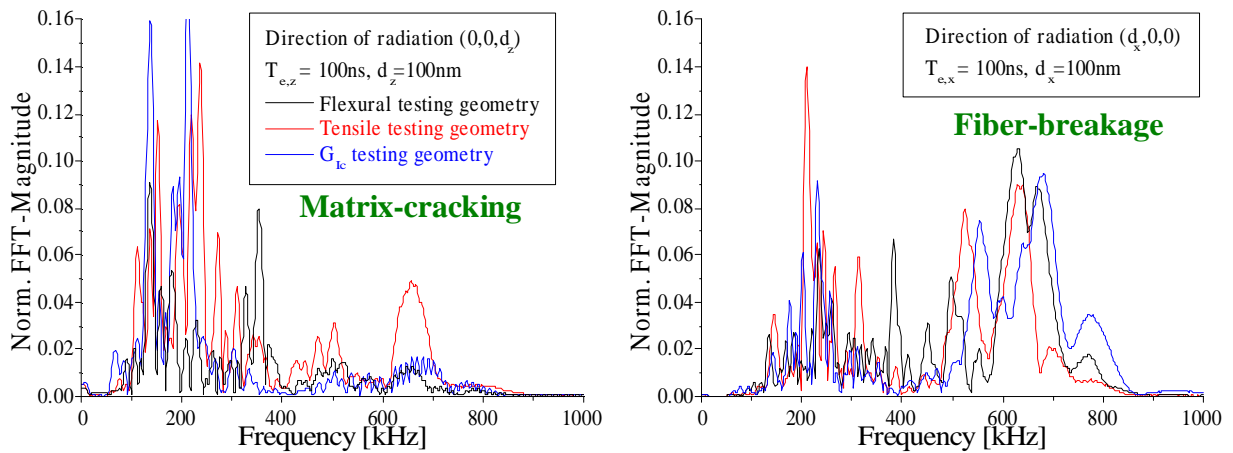


Fig. 4. Comparison of the simulated AE-signals frequency spectra for matrix-cracking and fiber-breakage at the $(x, y, z) = (0, 0, 0)$ position of the different geometries.

Pattern Recognition method

For investigation by pattern recognition, the frequency features summarized in table 3 are extracted from the recorded signals. The features numerical range was normalized by their variance and subsequently a principal component axis transformation was applied. The datasets then were partitioned using the cluster algorithm k-means. The suitability of the chosen feature settings, normalization procedure and cluster algorithm is based on a method proposed by [14] which uses cluster validity indices to evaluate the numerical quality of a dataset partitioning. As described in more detail before the numerical quality of discrimination can be evaluated by calculation of the parameters R and τ [6,15,16] as defined by [17] and [18].

$$R = \frac{1}{C} \sum_{i=1}^C \max_{i \neq j} \left(\frac{D_i + D_j}{D_{ij}} \right) \quad i, j = 1, \dots, C; \quad (\text{Eq. 1})$$

$$\tau = \frac{\min(D_{ij})}{\max(D_k)}; \quad i, j, k = 1, \dots, C; \quad (\text{Eq. 2})$$

Here D_i and D_j are defined as the average distance between members within a cluster and D_{ij} as the distance between the respective cluster centers. The index R is then calculated from the maximum values of R_{ij} divided by the number of clusters. The index τ is calculated from the minimal distance $\min(D_{ij})$ between members of clusters i and j and the maximum distance $\max(D_k)$ of members within cluster k . According to (Eq. 1) and (Eq. 2) the cluster members separate more distinctly for low values of R and high values of τ . Within the chosen approach an investigation of R and τ as a function of the number of clusters yields three clusters as numerical optimal value for partitioning of the signals. In figure 5a this is demonstrated for one representative investigation of a bending specimen. The respectively classified signals are plotted in figure 5b for one specimen as accumulated number of signals vs. time. For the three associated types of failure a significant shift in the acoustic emission onset is observed. Compared to matrix cracking and interfacial failure fiber breakage typically occurs at higher stress-strain levels. This is expected, since the initiation of failure in CFRP typically is caused by inter-fiber matrix cracking.

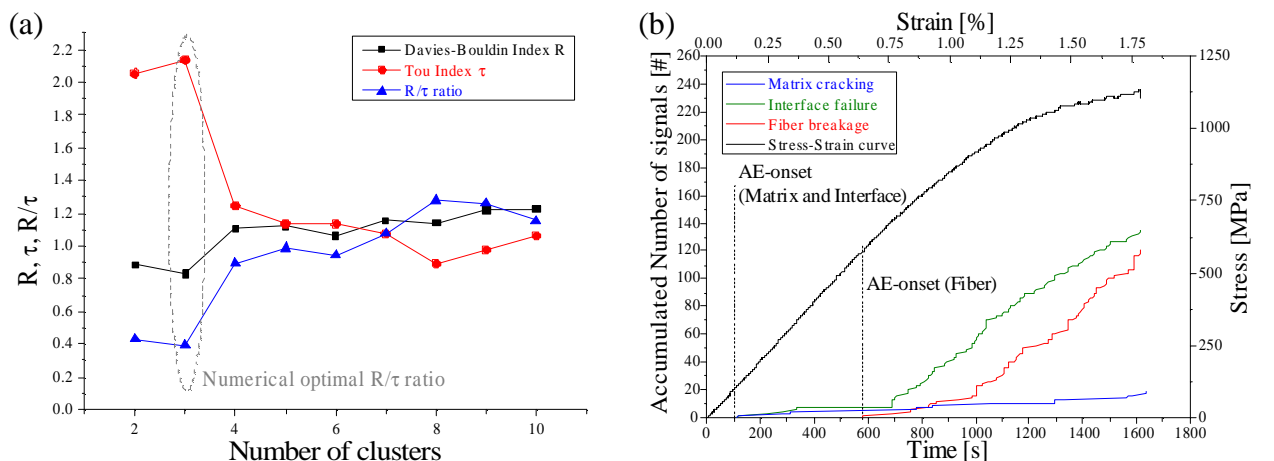


Fig. 5. Representative investigation of R and τ in dependence of cluster numbers (left) and result of classification from one representative bending specimen plotted as number of signals in dependence of time with respective stress-strain curve (right)

Table 3. AE-signal features used for pattern recognition approach

Peak-Frequency [Hz]	f_{\max} : frequency position of the max. frequency intensity
Weighted Peak-Frequency [Hz]	$\langle f_{\max} \rangle = \sqrt{f_{\max} \cdot \int f \cdot \hat{U}(f) df / \int \hat{U}(f) df}$ with $\hat{U}(f)$: FFT of $U(t)$
Partial Power 1-3 [%]	$\frac{\int_{f_1}^{f_2} \hat{U}^2(f) df}{\int_{0 \text{ kHz}}^{1200 \text{ kHz}} \hat{U}^2(f) df}$ Partial Power 1: $f_1 = 0$ kHz; $f_2 = 150$ kHz Partial Power 2: $f_1 = 150$ kHz; $f_2 = 300$ kHz Partial Power 3: $f_1 = 450$ kHz; $f_2 = 600$ kHz

Comparison between Pattern Recognition and FEM-Simulation results

Figure 6 shows the three distinct clusters of signals plotted in a Partial Power 3 vs. Weighted Peak-Frequency diagram. The plot emphasizes the distinct differences in the frequencies of the AE-signals and visualizes the positions of the different clusters. In addition, the positions of features extracted from simulated AE-signals are marked in figure 6. Here only the comparison concerning tensile specimens and G_{Ic} -specimens is shown. A similar comparison for the bending specimens is found in [6]. For the simulations of the different failure mechanisms the microscopically observed source positions were taken into account. For G_{Ic} -testing all failure mechanisms occur at almost constant vertical position $z = 0$, but show large variations in their x- and y-positions. Tensile testing results in fiber breakage within the 0° -layers only, while inter-ply delamination was dominantly observed at the interface between 0° and 90° -layers. Inter-fiber matrix cracking in turn occurs at distinct positions within the 90° -layers.

In summary the agreement between the simulated signals and associated clusters for the three different failure mechanisms is satisfactory. Only for interface failure, larger discrepancies between the simulated and the mean experimental values are observed. Since these types of signals are attributed to a variety of source mechanisms, the present source model should be generalized accordingly. In particular, all interface failure types were simulated with constant excitation times for all directions and constant displacement amplitudes d_x and $d_y=d_z$. Since these parameters influence the frequency characteristics of the respective signals they should be varied to fit the type of interface failure under investigation.

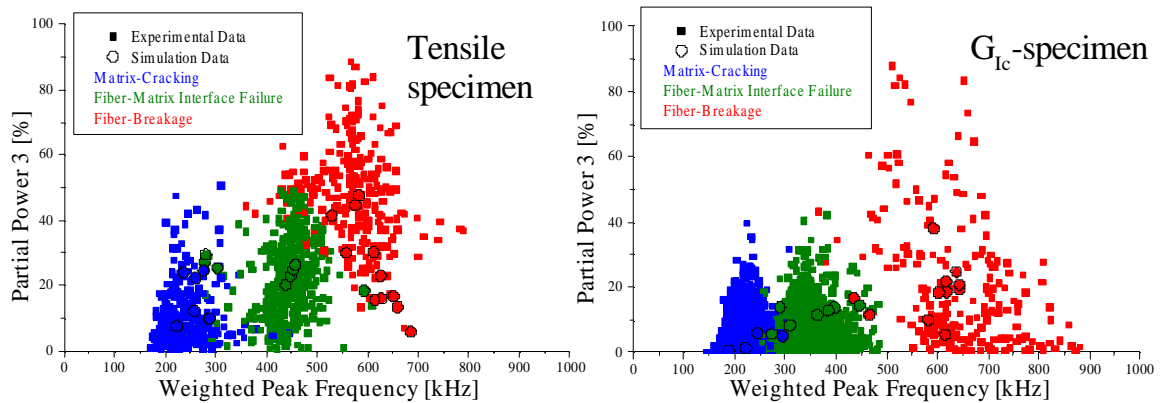


Fig. 6. Comparison of AE-signal features from simulated signals with respective cluster positions from pattern recognition approach for one representative tensile specimen and G_{Ic} -specimen.

Conclusion

Within the current investigation the proposed pattern recognition method applied to the acoustic emission signals recorded during mechanical loading yields distinguishable types of acoustic emission signals, which can be correlated with matrix cracking, interface failure and

fiber-breakage. The CFRP-specimen geometries investigated were implemented in FEM-simulations using an acoustic emission source model reflecting the microscopic situation of the various failure mechanisms and a model of a broadband sensor taking into account the sensor geometry and its frequency dependent sensitivity. In dependence of the source models position within the specimen volume, noticeable differences are observed in the simulated frequency spectra. The simulated acoustic emission signals show similar frequency parameter distributions as the experimental signals associated with the respective failure mechanism.

Although each specimen type shows characteristic frequency spectra due to the different stacking sequences and geometric boundary conditions, the simulated signals are still distinctly different for the different failure mechanisms in all experimental setups. Thus for matrix-cracking strongest contributions are observed below 400 kHz, while fiber-breakage results in frequency spectra with dominant contributions above 400 kHz. Interface failure typically shows frequency spectra, consisting of a combination of both contributions.

These findings support the suggestions of other authors that identification of particular failure types in CFRP based on frequency parameters is possible, but the identification process has to be reevaluated carefully for different geometries and stacking sequences than those investigated. In particular for larger specimen dimensions, the influence of dispersive signal propagation and attenuation has to be taken into account.

Acknowledgments

We thank A. Horoschenkoff and T. Müller from the University of Applied Science Munich for providing the specimens used in this investigation.

References

1. Bohse J., Chen J., *Journal of Acoustic Emission* **19**, 2001, p.1
2. Haselbach W., Lauke B., *Composites Science and Technology* **63**, 2003, p.2155
3. Ramirez-Jimenez C., Papadakis N., Reynolds N., Gan T., Purnell P., Pharaoh M., *Composites Science and Technology* **64**, 2004, p.1819
4. Marec A., Thomas J., Guerjouma R., *Mechanical Systems and Signal Processing* **22**, 2008, p.1441
5. Li X., Ramirez C., Hines E., Leeson M., Purnell P., Pharaoh M., *Proceedings of IEEE World Congress on Computational Intelligence*, 2008, Hong Kong, China
6. Sause M., Horn S., *Journal of Nondestructive Evaluation* **29** (2), 2010, p.123
7. Prosser W., Hamstad M., Gary J., Gallagher A., *Journal of Nondestructive Evaluation* **18** (3), 1999, p.83
8. Ohtsu M., Ono K., *J. Acoustic Emission* **5**, 1986, p.124
9. Castaings M., Bacon C., Hosten B., Predoi M., *Journal of the Acoustic Society of America* **115** (3), 2004, p.1125
10. Hamstad M., Gallagher A., Gary J., *Journal of Acoustic Emission* **20**, 2002, p.39
11. Bohse, J., 26th European Conference on Acoustic Emission Testing, Berlin, 2004, Germany.
12. Hatano H., Chaya T., Watanabe S., Jinbo K., *IEEE Transactions on Ultrasonics, Ferroelectrics and Frequency Control* **45** (5), 1998, p.1221
13. Goujon L., Baboux J., *Measurement Science and Technology* **14**, 2003, p.903
14. Anastassopoulos A., Philippidis T., *Journal of Acoustic Emission* **13**, 1995, p.11
15. Sause M., Schultheiß D., Horn S., *Journal of Acoustic Emission* **26**, 2008, p.1
16. Sause M., Haider F., Horn S., *Surface and Coatings Technology* **204** (3), 2009, p.300
17. Davies D., Bouldin D., *IEEE Transactions on Pattern Analysis and Machine Intelligence* **1**, 1979, p.224
18. Tou J., *International Journal of Computer and Information Sciences* **8** (6), 1979, p.541